

Author response to the reviews of the manuscript:

We first would like to thank both reviewers for their detailed reviews and the very encouraging remarks to this manuscript. We appreciate the recommendations in form and content; which we generally accepted – this has led to a considerable improvement of the paper.

Response to comments of reviewer 1:

Although; the reviewer in his final statement requests only minor textual changes, we feel some of the comments are too important not to be discussed in more detail. Regarding the comments pertaining to the figures, we followed the recommendation to brighten the colormap in Figure 8, such that the contrast of the vector field is enhanced and the circulation is better visible. We further changed the internal labels in Figure 3 to **mean velocity** and to **eddy velocity** and now use a blue color shading for the topographic slope along the steep areas of the bathymetry.

The reviewer asked for some substantial alterations which we will discuss in the following:

- **RC1 a)** The reviewer identified the derivation of the Peclet Number as the only scientific contribution of the paper.
- **AR1 a)** In fact, we feel that the estimation of a mid-depth EKE field is the major finding and has important scientific consequences for the distribution of mid depth water masses in circulation system with sufficiently different regimes of advection and diffusion at mid depths. The Pe , as it is estimated here, should be seen as a relative (qualitative) quantity that allows to detect regional differences in the advection/diffusion distribution at mid-depth (also recommended by reviewer 2).
- **RC1 b)** The reviewer requested more details about the underlying dataset (YoMaHa) particularly with regard to biases that may occur during the profiling time of the floats.
- **AR1 b)** Sources of uncertainties are in fact manifold, and we elaborated on that subject in the paper and extended that discussion. We also included the underlying technical report (Lebedev et al., 2007) in which some of the error sources are also discussed.
- **RC1 c)** The reviewer requested to directly put the geographical locations inside the text, even when listed in the Table.
- **AR1 c)** We agree that there should be better guidance to some of the locations, but we feel just giving lat/lon data are less illustrative than for example a more descriptive note: (mooring CIS located in the center of the Irminger Sea). However, this is for mooring locations that are part of the Table and included are geographical locations. For other locations like OWS Bravo and 'Orphan Knoll' we included lat/lon in the text as recommended.
- **RC1 d)** The reviewer requested some additional references. He argued that such a well-documented region requires some additional references of both observational and numerical studies.
- **AR1 d)** Thus, we added several additional citations.

Author response to the comments of reviewer 2:

In addition to the textual remarks, the reviewer raised several substantial remarks, which we thoroughly address.

RC2: The reviewer was surprised that the authors chose to merge the 1000 m and 1500 m float displacements (Line 143) without doing any thermal wind adjustment, and the concern would be a bias in both the mean and the eddy field if such an adjustment is not done.

AR2: Indeed we had a discussion about a thermal wind adjustment earlier in the writing phase of the manuscript, and we re-discussed this concern with respect to the remarks of reviewer 2. We came to the following conclusions: for various reasons, discussed below, we will not use any geostrophic adjustment, but we agree that more details are needed to convince the reader that joining the data from the two depth levels is appropriate.

Thermal wind shear adjustment of individual data (displacement vectors) would need synoptic measurements of T/S profiles in the vicinity of the data point. Argo trajectory data of individual floats are synoptic, but would only support the cross – component, and with the concept of f/H following flow this would correspond to cross-bathymetric flow; near the topography this is generally small compared to boundary current speeds. In order to estimate the perpendicular velocity component one would need simultaneous T/S profiles from near-by floats. Within time scales of days to month this is rarely the case.

The second possible version is to map the T/S field and calculate the mean shear on a similar grid. Based on the high resolution MIMOC climatology the effect is small in the western SPNA, and it is only the southeastern SPNA where the shear is stronger due to the presence of the more baroclinic NAC. Thermal wind adjustment based on this mean T/S-field will mix time and space variations in an arbitrary manner and can only be applied to the mean velocity field. In consequence it would not be possible anymore to separate the raw data into u' and $\langle U \rangle$ components.

However, there is other information that may be used as justification for combining the data from both levels. First, we inspected current shears from moored records from both, the boundary current regime (Fischer et al., 2010, for mean velocity profiles in the DWBC in the Labrador Sea; Fischer et al., 2015 for the DWBC at various place around the SPNA) and interior flow (Figure 7 of the manuscript). From the Argo data we performed the gridding procedures for both depths independently, but with lower resolution and larger interpolation radii. The fields from the 1000m floats resemble that of the final product and there are no large scale biases (basin wide means). This is different for the 1500m floats where the data coverage is smaller and there are several large gaps. In general, the flow field along the topography will be different because the shallower level between 1000 and 1500m depth is only represented by the 1000m field.

There were some areas in which the data density appeared large enough in both fields; e.g. southern Labrador Sea and Irminger Sea (see attached figure 1):

For the Irminger Sea, an area with boundary currents, interior advection, and sluggish circulation, we find rather similar circulation patterns in both levels. Beside

the two levels we include the velocity difference of the 1000m level minus the 1500m velocity (right subplot of figure 1) with the largest differences in areas of low data density, e.g. along the DWBC off East-Greenland. We obtained the following statistical values (see table) with the individual means being much larger than the mean difference. The standard deviation of individual components are also larger than the standard deviations of the difference field. This supports the conclusion that a statistical significant difference is not detectable and that we may combine the two fields into a single layer without any adjustment.

Field	Mean (cm/s)	Standard Dev (cm/s)
U1000	-0.90	2.45
V1000	-0.55	3.17
U1500	-0.78	2.86
V1500	-0.64	3.24
U10-U15	-0.12	1.60
V10-V15	0.09	1.77

RC2: The reviewer has some concern about the interpretation of the Peclet number as a quantitative measure of advection vs. diffusion.

AR2: We totally agree on this point and would also see the Peclet number as it is defined here in a rather simplistic way as a qualitative rather than a quantitative measure. Thus we interpret the regional differences in the Pe distribution as regional variations of the relative importance of advection and diffusion. This is now made clearer in the manuscript.

RC2: Finally, it is not clear which altimetry product was used. If it is the gridded product, it should be noted that it has much lower EKE than that produced from an along-track product (Zhang and Yan 2018). Thus, the comparison of the surface and deep EKE might have fewer regions with deep EKE > surface EKE. The overall interpretation of Figure 8 need not change, but I believe a note regarding what size eddies the altimeter product resolves is in order.

AC2: We used the gridded altimetric product which has a horizontal resolution of 0.25° -- comparable to the resolution of the grid used herein. However, as the typical eddy size in the subpolar area is of similar size (10 to 50 km), the EKE estimates are certainly biased low compared to estimates of EKE from the along-track records. Thus, the ratio of the top to deep EKE should not be seen as an absolute measure, but for identifying regional differences between deep and surface EKE fields. This is now better explained in the text.

RC2: Line 194 - I don't see how the three float trajectories plotted on top of the mean flow field is an indication of how well the PV-constraint works

AC2: The trajectories show that individual floats stay for a long time (up to years) in a narrow bathymetric depth range which is indicated (figure 3a) through the colored topographic range. While the Coriolis force (f) does not change much along the trajectories this behavior is an indication that the floats indeed follow the bathymetry and therefore f/H as a measure of the large scale potential vorticity.

RC2: All data within a radius of 110 km and at locations with similar water depths – less than 1000m difference – were used in the OI." How was 1000 m chosen? Were there any sensitivity tests that informed this decision?

AC2: The rationale behind the choice of the cut-off radii was twofold: first, across the boundary currents the bathymetric slope is of the order of 2000m and we would not like to smear out the boundary currents by more than half of its width. This was similar to the parameters chosen for the Gaussian interpolation (GI) method. For the GI we performed some variational tests with the interpolation scales including the cut-off radii. The chosen parameters were a compromise between resolution and smoothness of the resulting fields.

RC2: Is Figure 3 made using the gridding procedure with a penalty in the cross-isobath direction? It would be helpful to point toward the exact subsection in the text where plotting procedure is described in the Figure caption. If this procedure is used, then it seems circular to argue that the coherence of the velocities along isobaths.

AC2: This is an important point – we used the cross isobaths penalty for generating Figure 3a, and based solely on this field it is in fact circular to conclude on along isobaths coherence. However, this coherence still exists when the cross isobaths penalty is removed; although the boundary currents are becoming wider through spreading towards the basin interior. This is now stated in the text.

RC2: Line 395ff - The manuscript goes through the exercise of comparing the two mapping methods (GI and OI). In this comparison, it comes to light that de-spiking to remove the top 1% of the largest velocities as part of the GI method, increases the bias relative to the OI method by 400%. This seems like a cautionary tale for users of each method, but the authors stop short of explaining how to avoid biases from anomalous velocities. It would be useful for the authors to give a more extended judgement on the promises and pitfalls of each method.


AC2: In fact any of the mapping procedures requires some despiking of the velocities (especially the eddy component has some spikes close to the bathymetry, see Figure 3b). These are treated differently in the respective method. While the OI method uses least square techniques in which individual spikes have little influence, the GI method uses the data more directly, and for grid points close to the spike position these get a strong weight, such that the EKE is biased low. The magnitude of this bias depends

on details of the editing method. When a simple sort and remove procedure is used then the bias increased from $1 \text{ cm}^2 \text{ s}^{-2}$ to $4 \text{ cm}^2 \text{ s}^{-2}$. Adding additional statistic constraints (e.g. removal only values exceeding 2-standard deviations within the area used for the interpolation --- order 100km range) would reduce the bias to the range of $1\text{-}2 \text{ cm}^2 \text{ s}^{-2}$. However, we agree that a quantitative interpretation of the EKE and local variations of it should be made cautionary. This extended description is now incorporated in the text.

RC2: - This study does not look at flow at the Grand Banks, and southward flow around Flemish Cap appears strong in Figure 3 and 5a, with relatively high Pe in Figure 5c. Therefore, I do not understand the evidence provided in support of this conclusion: "While the Irminger Sea route appears strong and robust, the flow along the topography (Flemish Cap and Grand Banks) is relatively weak." I suggest removing this sentence or including some references to support it.

AC2: This has been rewritten with a not so rigid statement regarding the Flemish Cap pathway, and we added the reference (Schott et al., 2004) that has a focus on the circulation along the Grand Banks.

Fischer, J., Karstensen, J., Zantopp, R. J., Visbeck, M., Biastoch, A., Behrens, E., Böning, C. W., Quadfasel, D., Jochumsen, K., Valdimarsson, H., Jónsson, S., Bacon, S., Holliday, N. P., Dye, S., Rhein, M. und Mertens, C. (2015) [*Intra-seasonal variability of the DWBC in the western subpolar North Atlantic*](#). Progress in Oceanography, 132 . pp. 233-249. DOI [10.1016/j.pocean.2014.04.002](#).

Schott, F., Stramma, L., Zantopp, R. J., Dengler, M., Fischer, J. und Wibaux, M. (2004) [*Circulation and deep water export at the western exit of the subpolar North Atlantic*](#).  Journal of Physical Oceanography, 34 . pp. 817-843. DOI [10.1175/1520-0485\(2004\)034<0817:CADEAT>2.0.CO;2](#)

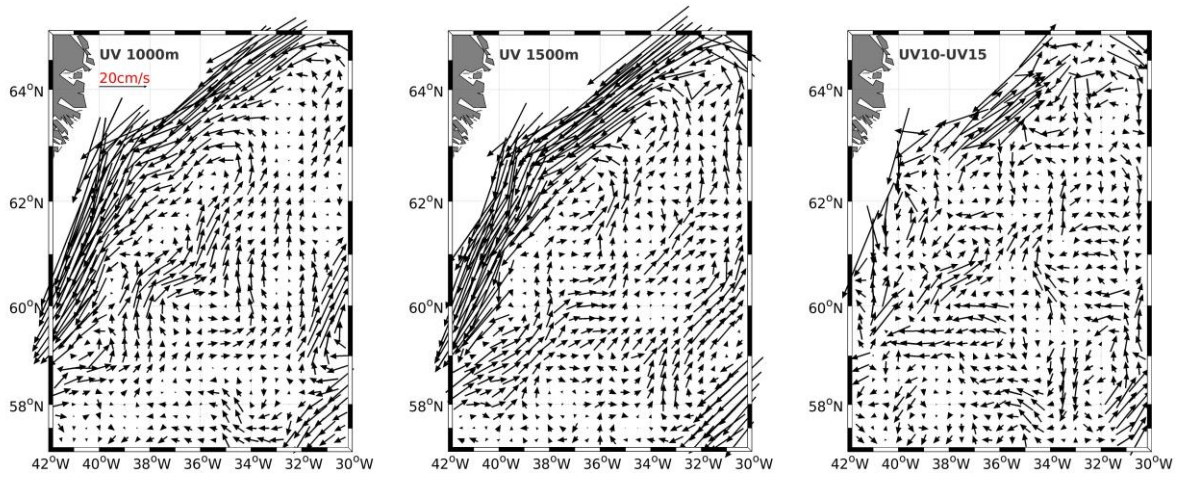


Figure 1: Comparison of the mean flow from subsets of the data: left the flow in 1000m depth; middle the flow in 1500m depth, and right the difference of the two fields.

Mean circulation and EKE distribution in the Labrador Sea Water level of the subpolar North Atlantic.

Jürgen Fischer¹, Johannes Karstensen¹, Marilena Oltmanns¹, Sunke Schmidt¹

5 ¹GEOMAR Helmholtz Centre for Ocean Research Kiel, Düsternbrooker Weg 20, 24115 Kiel

Correspondence to: Jürgen Fischer (jfischer@geomar.de); Johannes Karstensen (jkarstensen@geomar.de);

Feldfunktion geändert

Feldfunktion geändert

10 **Abstract:** A long term mean flow field for the subpolar North Atlantic region with a horizontal resolution of approximately 25 km is created by gridding Argo-derived velocity vectors using two different topography following interpolation schemes. The 10-d float displacements in the typical drift depths of 1000 m to 1500 m represent the flow in the Labrador Sea Water density range. Both mapping algorithms separate the flow field into potential vorticity (PV) conserving, i.e. topography following contribution and a deviating part, which we define
15 as the eddy contribution. To verify the significance of the separation, we compare the mean flow and the eddy kinetic energy (EKE), derived from both mapping algorithms, with those obtained from multiyear mooring observations.

The PV-conserving mean flow is characterized by stable boundary currents along all major topographic features including shelf breaks and basin-interior topographic ridges such as the Reykjanes Ridge or the Rockall Plateau.

20 Mid-basin northward advection pathways from the northeastern Labrador Sea into the Irminger Sea and from the Mid Atlantic Ridge region into the Iceland basin are well-resolved. An eastward flow is present across the southern boundary of the subpolar gyre near 52°N, the latitude of the Charlie Gibbs Fracture Zone.

The mid-depth EKE field resembles most of the satellite-derived surface EKE field. However, noticeable differences exist along the northward advection pathways in the Irminger Sea and the Iceland basin, where the deep EKE exceeds the surface EKE field. Further, the ratio between mean flow and the square root of the EKE, the Peclet Number, reveals distinct advection-dominated regions as well as basin interior regimes in which
25 mixing is prevailing.

Keywords:

- 30
- Subpolar North Atlantic
 - Intermediate depth EKE
 - Subpolar mid-depth advection
 - Argo data, OceanSITES data
 - Ocean model metric
- 35

40

1 Introduction

45 The subpolar North Atlantic has been in the focus of both observational and modelling efforts ~~in hindsight~~
~~with regard~~ of circulation- and water mass changes as part of the climate relevant Atlantic Meridional Overturning
Circulation (AMOC; reviewed e.g. by Daniault, et al., 2016). In this context the intermediate depth circulation,
which also determines the spreading pathways of newly ventilated Labrador Sea Water (LSW) through the
subpolar North Atlantic (SPNA), is of specific importance and has been investigated from observations and
50 models for several decades. A better understanding of the mechanisms that control the transport properties at mid
ocean depth through the interplay of advection and diffusion is fundamental to our understanding of subpolar
LSW circulation and export, and thus potentially subpolar AMOC contributions. Unlike the surface circulation,
which can be analyzed for example from satellite and drifter data, the intermediate depth circulation and
energetics is known to a much lesser extent. Studies that map energetics at the intermediate depth from
55 observational data and at gyre scales are rare but identified for example as important evaluation metrics for basic
verification of ocean model simulations, including CMIPs models (Griffies et al. 2016).

In the late 1990~~ies~~, technology of profiling floats advanced such that investigations of the intermediate deep
circulation could be undertaken. Two experiments were carried out in the western subpolar North Atlantic
(mainly in the Labrador- and Irminger Seas) using Profiling ALACE (PALACE) floats and are of special interest
60 to the investigation carried out herein. The first was by Lavender et al. (2000) with a large fleet of floats drifting
through the Labrador and Irminger Seas in 700m depth (the approximate depth level of upper Labrador Sea
Water in the subpolar North Atlantic). A major result of the study was that the intermediate depth circulation
could well be described as a cyclonic boundary current system along the topography and a series of anticyclonic
recirculation cells adjacent to the Deep Western Boundary Current (DWBC). The second experiment was
65 dedicated to the boundary current off Labrador, and conducted in summers 1997 and 1999 with 15 PALACE
floats seeded into the DWBC off Labrador to drift at 1500m, the core depth of classical LSW (Fischer and
Schott, 2002). The main finding of this study and contrary to the expectations was that none of the floats was
able to exit the subpolar gyre via the boundary current route. Instead, some of the floats confirmed the existence
of a recirculation cell off Labrador and others indicated an eastward route following the North Atlantic Current
70 at its northeastern pathway. This result stimulated a series of Lagrangian experiments (Bower et al., 2009) using
RAFOS drifters but also model studies (e.g., Spall and Pickart, 2003).

With the deployment of the global array of Argo profiling floats at the end of the 1990s the number and spatial
homogeneity of displacement vectors at the floats parking depth of typically 1000 m or 1500 m increased
75 significantly. The data set is assembled in the YoMaHa'07 data base (Lebedev et al., 2007). Based on this much
larger database it is of interest to revisit the earlier results. One of the immediate questions is how robust the
earlier findings are, and moreover whether the present day Argo data coverage would be sufficient to ~~prove~~
and possibly refine the earlier results. There are two approaches to these objectives, one is to investigate
temporal changes of the deep circulation on interannual time scales but with a drawback on spatial resolution.
80 Palter et al., (2016) followed that approach and found a slowdown in boundary currents flow in the Labrador Sea
but no significant changes in the large scale subpolar gyre circulation. Another approach, and this is taken here,
is to neglect temporal variability and use all available displacement data for determining a mean flow field on a

finer spatial resolution that resembles narrow circulation elements in higher resolution compared to what have been discussed in the past.

85

Several attempts have been undertaken to estimate advective (long term mean) and diffusive contributions in the displacement vectors on the basis of statistical and physical constraints. While the displacements of the profiling floats may be well suited to determine the long term mean of the flow field, this is not straight forward for the eddy component of the flow field (Davis, 2005). The author suggested calculating the diffusivity from displacement anomalies \mathbf{u}' calculated from the difference of the mean flow $\langle \mathbf{U} \rangle$ and the measured displacement vector \mathbf{U}_m . Here, we loosely follow the method proposed by Davis (1991), in which the mean flow is controlled by topography (f/H , with H is the water depth), an assumption that should hold true in the SPNA regime where weak stratification and small vertical current shear is encountered. Thus, we will estimate the advective part of the flow that is related to the concept of potential vorticity conservation (LaCasce, J.H., 2000), and the residual flow contribution that is attributed to the diffusive part of the flow. Validation of this principle has been performed in the past (see Fischer and Schott, 2002; Fischer et al., 2004) through a comparison of deep displacements along curved topography in relation to moored (Eulerian) records.

90

95

We focus here on the SPNA north of 45°N and make use of the extended set of Eulerian (current meter moorings) and Lagrangian (floats) observations available in the region. Over the previous two decades (regionally even longer) an impressive observing effort has been undertaken north of 45°N on the (intermediate) deep flow. Boundary currents are, thanks to their strength, the prominent circulation features in the SPNA and found all along the shelf edges in particular on the western side of the gyre. However, there are also interior circulation features of both advective- and eddy-dominated pattern, and the primary research objective of this effort is to discriminate the mean flow $\langle \mathbf{U} \rangle$ from the turbulent (eddy) component \mathbf{u}' of the flow field from which the deep EKE field could be determined.

100

105

The paper is structured [as follows](#): First, we briefly describe the methods to separate $\langle \mathbf{U} \rangle$ and an accompanying \mathbf{u}' , obtained for each displacement vector from the difference between the observed displacement and the displacement projected to a PV contour. The fields obtained by two different gridding methods are verified for internal consistency, and in comparison to independent measurements from mooring records. Next, a gridded velocity and an Eddy Kinetic Energy (EKE) field of relatively high spatial resolution (order 25km grid size) for the SPNA is created by both gridding procedures. We discuss the fields for internal consistency based on major flow features. Furthermore, the ratio of advective flow and diffusion (Peclet number) is estimated. The EKE field at depth is then compared with the EKE field at the surface, based on satellite data. The gridded data sets are provided for download and further use e.g. for model/data comparison, so far we are not aware of an intermediate depth EKE map.

110

115

2 Material and Methods

Two quality controlled Argo displacement (deep and surface) sets exist, but cover somewhat different time spans. Here, we use the [YomaHha07](#) - Argo dataset (Lebedev et al., 2007) which contains estimates of

120

velocities of deep and surface currents using data of the trajectories from displacements between consecutive dives of Argo floats. The YoMaHa'07 data set is updated frequently on a monthly basis.

This technical paper contains most of the necessary processing stages for both the deep and the surface velocity. There is also some discussion regarding the error sources arising as a consequence of the 3-dimensional measurements; in this report there is a discussion on the error assessment of deep velocity due to vertical shear of horizontal flow. While the floats are ascending from their drift, they will be subject to the flow field in the water column. In a weakly sheared environment like the subpolar North Atlantic this effect is considered to be small. However, there is a much larger error source that is due to calculating straight line displacement vectors, which in the presence of curved bathymetry is large and it is a bias. This is illustrated by the following example of the DWBC surrounding Hamilton Bank near 55°N off Labrador. A float that travels in this area at a mean speed of 15cm s⁻¹ will surround Hamilton Bank within one or two dive cycle of the float. The difference of a straight line displacement and the displacement estimated from the length of e.g. the 1500m isobath can be different by about 30% ; Thus, the straight line displacement is biased low especially in areas of high velocities and curved topography, e.g. the DWBC..

Formatiert: Englisch (USA)

Formatiert: Hochgestellt

Formatiert: Englisch (USA)

This data set is updated frequently on a monthly basis.

2.1 Temporal and spatial distribution of the Argo float array

By March 2017 (this is the latest data considered for this analysis) the displacement data set includes data from 4284 floats stored in nine Data Assembly Centers (DAC's) worldwide and about 297,000 values of velocity. We define a velocity vector as the displacement between an Argo float descent (last surface position) and the consecutive ascent (first surfacing position) divided by the corresponding time difference. Some inhomogeneity in position and time accuracy based on the communication and positioning technology (ARGOS, Iridium) is discussed in Lebedev et al. (2007). The nominal position of the velocity vector is the mean position between the descent and ascent position pair.

The area under investigation ranges from 45°N, the latitude just south of Flemish Cap, to 65°N, which is just south of Denmark Strait (Figure 1). The westernmost longitude is 62°W, i.e. the Labrador shelf break, and to the east, the area is bounded at 7°W west of the British Isles. The evolution of the Argo data in this domain shows a rapid increase in data density in the first 5 years of the program (**Figure 2**), and from 2006 onwards the data density is adding around 2500 to 3000 displacement vectors per year; this is roughly equivalent to the number of T/S profiles gained through Argo per year. Maximum annual data increase is reached in 2011/12 with 4000 additional current vectors each year. Thereafter, the yearly data gain stabilizes at 2500 to 3000 current vectors.

The regional data density ranges from approximately 10 to more than 100 per bin (2°longitude x 1° latitude; **Figure 1**); the bin size corresponds with the typical area in which data will be used for the interpolation to a certain grid point. Given the barotropic nature of the flow field in the SPNA we merged the displacement vectors from the two drift depths 1000m and 1500m depth. Considering the temperature and salinity data recorded by the floats the mean potential density field at 1500 m varies between $\sigma_\theta = 27.72 \text{ kg m}^{-3}$ and 27.92 kg m^{-3} with an average density of $\sigma_\theta = 27.77 \text{ kg m}^{-3}$. This density is slightly lower than the commonly used lower boundary of classical LSW at $\sigma_\theta = 27.80 \text{ kg m}^{-3}$ and thus, the resulting circulation pattern represents the core depth of the LSW.

2.2 Auxiliary data

165 To estimate contours of constant potential vorticity defined as (PV/Coriolis parameter divided by waterdepth (f/H)) we used the high resolution topographic data 2-minute Gridded Global Relief Data (ETOPO2) (National Geophysical Data Center, 2006). This topography is based on a combination of depth soundings and depth estimates from multiple sources and gridded to a 2-minute special resolution. Only in one case we use the higher resolved ETOPO1 version, but this did not change the results.

170 Furthermore, we used altimetry-based absolute dynamic topography from which the surface geostrophic flow and EKE were derived [Le Traon et al., 1998]. The altimeter products were produced by Ssalto/Duacs and distributed by Aviso with support from Cnes (<http://www.aviso.altimetry.fr/duacs/>). We used the gridded product with a 0.25° horizontal resolution, similar to the resolution of the deep velocity field. We note, however, that the surface EKE, derived from this product, will be biased low as subgrid-scale variability is smoothed out.

175 Lastly, Eulerian time series data from moored instrumentation that recorded in the depth interval considered in the analysis here (1000-1500m) were used to locally evaluate the results of the gridded data product (see table 1 for an overview). Given the floats inherent sampling at 10 days, the moored records were smoothed accordingly.

180 2.3 Separating mean flow and its fluctuation and interpolation of the results

Two interpolation methods were used to map the displacement vector data: the first is a weighted Gaussian interpolation (GI) and the second is an optimum interpolation (OI) procedure. Both methods use the same physical constraints, and both operate on an identical grid of 0.5° longitudinal range and 0.25° latitudinal range.

2.3.1 Gaussian interpolation method

185 The strategy of the GI-method was to include two constraints in the interpolation procedure, namely a weighted distance between target (grid) point and data point, and the second is to reduce the influence of data points located in regions with very different water depth. The latter is a manifestation of our assumption that flow in the region follows PV-contours. Thus, data points across the boundary current at steep topography would only
190 weakly be influenced from nearby but much deeper/shallower locations outside the boundary current (a topography following mapping).

The weights used have a Gaussian shape described by two parameters for each dimension: for the distance weighting we chose 40 km for the half width of the Gaussian and 80km for the cut-off – such that points outside a radius of ~80km around a selected grid point will not be used. For the other dimension (water depth difference
195 between data location and target location as a measure of PV difference) we chose 200 m half width and 600m cut-off range. The choice of these values was guided by the dimensions of the boundary current along steep topography (e.g., the Labrador shelf break), with the width of the DWBC (Zantopp et al., 2017) between 100 km and 150 km, and a change of water depth across the DWBC from about 1000m to 3000 m. Through this procedure Boundary Currents would be conserved and not smeared out, while in the basin interior with flat
200 bottom the weight is more toward distance – with only little influence of the underlying bathymetrydepth-difference.

We analyzed the impact of different weights over a wide range of scales, but the selection applied here appears to generate the most robust result with a clear definition of the circulation elements described hereafter. Using a higher resolved grid (smaller scales) results in a noisier flow field with larger overall variance, while a coarser grid (together with larger interpolation scales) results in a smoother field and certain details of the flow field are suppressed. The procedure could be applied to both irregular target locations, and regular grid locations.

In a first processing step we separate the measurements into a mean flow contribution $\langle U \rangle$ and a fluctuating part u' that will be used later to determine the EKE field. Around each measurement location we selected all data within the cut-off radius and by using the selected weights (see above) we estimate a mean flow vector at the measurement location by applying the above described algorithm. Thus, we generate a velocity field that has the dimension of the original data set, and it contains only the weighted, PV-related ensemble-mean contribution (Figure 3a). As an illustration ~~how well the PV-constraint works~~ we show three floats that were deployed at roughly the same location in the northern Iceland Basin at water depth around 1800m to 2500m. The length of the trajectories correspond to more than two years elapsed since deployment. The floats stayed within that depth range for a significant fraction of that time. This depth range is shaded all around the basin, and and the close correspondence of the float trajectories and the shaded area is an indication of the PV following nature of the deep flow field.

~~By subtracting the mean component, which we assume to be inherent in each of the measured displacement vectors, from the original data a current residual (u') could be calculated (Figure 3b).~~

Subsequently we applied the mapping procedure to the measured velocity field (U_m) to obtain a field on a regular 0.5° longitude x 0.25° latitudinal grid and the result is $\langle U \rangle$ on a regular grid, which is considered as one of our final data products.

After estimating the mean velocity from the displacement vectors, we calculated the residual flow components (u' and v') by subtracting the mean component from the original data (Figure 3b).

The eddy kinetic energy (EKE) is estimated independently for each of the two interpolation methods (GI and OI). Assuming that the separation of the measured displacement vectors into $\langle U \rangle$ (advective) and a fluctuating (eddy) component is successfully performed by the above methods, it allows to calculate u' and v' , the fluctuating (eddy) velocity contribution of each displacement vector (Figure 3b). Both eddy-components show similar overall (basin wide) statistics of Gaussian shape and equal rms-values of 4.9 cm s^{-1} (Figure 4). The second final data product is the gridded EKE produced from the u' and v' fields derived through the first interpolation step.

2.3.2 Optimum Interpolation method

The second procedure uses the method of optimum interpolation (OI-method), similar to the one described in detail in Schmidt et al. (2013). Data was only mapped if the grid points have a water depth deeper than 1200m according to the topographic data set. All data within a radius of 110km and at locations with similar water depths – less than 1000m difference – were used in the OI. Linear gradients in latitudinal direction, longitudinal

240 direction and water depth were fitted to the data. For the covariance matrix a diagonal value of 1.5 was used as
an estimate for the signal to noise ratio (see Schmidt et al. 2013 for details). The background field used in the
optimal interpolation was taken from a least squares linear and quadratic fit of the data using depth, longitude
and latitude.

245 The field, resulting from the OI was used as mean flow field $\langle U \rangle$ which was then used to compute the residual
flow (u' and v') from each displacement vector (U_m) by linear four point interpolation. An individual EKE value
was computed for each displacement. To exclude extreme outliers an inter quartile range filter was applied,
rejecting data points 2.2 times the inter quartile range above the third quartile or that range below the first
quartile. This is similar to a 99.98% standard deviation filter in case of normal distributed data. The EKE data
was then mapped in an identical procedure as the mean field.

3 Results

250 3.1. The intermediate depth large scale circulation from a displacement vector point of view

First we inspected the GI based interpolation of $\langle U \rangle$ on the original displacement vector positions which
represents individual mean flow realizations and added a number of selected float trajectories (**Figure 3a**). The
flow realizations nicely sample the different flow regimes in the SPNA and cover the boundary currents; flow
associated with topographic features, such as the Mid-Atlantic Ridge; prominent flow features, such as the deep
255 extension of the North Atlantic Current in the 'North West Corner'. Selected areas are discussed in the
following.

3.1.1 Boundary Currents

260 Individual mean flow realizations sample the boundary currents and indicate the coherence of the flow along the
topography. This is also confirmed by individual float trajectories. Individual floats that were released in the
northern Iceland Basin, near the northernmost part of the Reykjanes Ridge (RR), follow the deep boundary
current along the topographic slope of the RR south-westward. The displacement vectors indicate swift speeds of
approximately 6 to 7 cm s⁻¹. For the selected floats it takes about 3 month to reach the first gaps in the RR and
thus to enter the Irminger Basin. However, different gaps exist and ~~control~~-influence the exchange with the
265 Irminger Basin. After crossing the RR the floats take a northward drift on the western side of RR in the boundary
current that surrounds the northern Irminger Sea and downstream merge into the deep East Greenland Current
(dEGC). The selected floats stayed for almost two years in the deep boundary current inshore the 1800 m
isobaths before they reached Cape Farewell, the southern tip of Greenland and which is about 2500 km
downstream (comparable with a mean drift speed of about 4 cm s⁻¹). At about the latitude of Cape Farewell, the
270 northward flow along the western flank of the RR is on the order of 5 cm s⁻¹, while the southward flow along the
east Greenland shelf break regionally exceeds 10 cm s⁻¹. The trajectories clearly show that the PV (depth)
constraint on the flow is very strong and as such our gridding procedure appropriate.

3.1.2 Labrador Sea

275 The intermediate circulation in the Labrador Sea shows narrow cyclonic boundary circulation where the topography is steep, i.e., along the East Greenland – and Labrador shelf breaks (**Figure 3a**), while in regions with a gentler slope (e.g. northern part of Labrador Sea) the boundary current widens considerably. From the boundary current to the interior Labrador Sea the flow reveals stable but weak recirculation cells with cyclonic rotation, and the interior of these elongated cells is almost stagnant, as is also seen in time series measurements
280 (Fischer et al., 2010;) [of the 53° moored array](#) at location K10, where the mean 1500 m-flow is 0.8 cm s^{-1} northwestward, and at K9 where the mean flow is 12.5 cm s^{-1} but southeastward (**Figure 5b; Table 1**).

The nearly stagnant, weakly anticyclonic ~~rotation-circulation~~ is observed for the area where deep convection takes place. Here the water is trapped within the closed circulation in the region of strong wintertime buoyancy loss. Both, the cyclonic recirculation cells along the Labrador shelf break, and the anticyclonic interior are thus
285 favorable for deep convection. At 1500 m depth, the lightest water is found in the central Labrador Sea and is surrounded by extremely weak ([order 1cm/s](#)) anticyclonic flow. Eventually the water in the central Labrador Sea feeds the advective path around Cape Farewell thereby exporting light and weakly stratified water into the Irminger Sea. Further south, at the exit of the Labrador Sea the flow enters a very active eddy regime in a region with very variable topography – the ‘Orphan Knoll’ region [near 47°W, 51°N](#). Here the North West Corner of the
290 NAC and the outflow of the Labrador Sea merge and interact.

3.1.3 Irminger Sea

295 | The Irminger Sea has several characteristic flow patterns in intermediate depth (**Figure 3a**). The most
pronounced feature is the deep East Greenland Current (dEGC) that exists over the whole western part of the
basin. On the opposite side the Irminger Sea is bounded by the Reykjanes Ridge that is a barrier for most of the
flow beneath 1000m depth. Further south, several gaps in the ridge allow the water from the eastern basin to
spill over the ridge and a northward deep boundary current forms along the western flank of the ridge. This is
one source of the dEGC. A second source of the intermediate dEGC is the mid-basin current band that is fed
300 | from the Labrador Sea and extends up to 64°N where it enters the dEGC; the cyclonic circulation that this mid-
basin vein forms is sometimes called the Irminger Gyre. Within the Irminger gyre a number of long term
moorings have been maintained for more than a decade to record the thermohaline evolution of the gyre center
and possibly deep convection underneath the Greenland Tip Jet (e.g. Pickart et al., 2003); the moorings are
nowadays incorporated in the international OSNAP_ ([Overturning in the Subpolar North Atlantic Program](#))
305 | program ([Lozier et al., 2016](#)) and the OOI ([Ocean Observatories Initiative, http://ooinet.oceanobservatories.org](#))
initiative. The mid-basin current band appears to have a number of meanders which are also visible in the
1500m geopotential derived from the Argo profile data.

3.1.4 Iceland Basin

310 | The Iceland Basin, which is less well investigated, has two major topographic features that influence the
circulation strongly. The western limit of the Iceland Basin is the RR and that show the already discussed
boundary current. At the location of the Charlie Gibbs Fracture Zone (CGFZ), which is at about 52°N, forms
dynamically the southern boundary of the basin and where the circulation at the LSW depth is eastward in
connection to the North Atlantic Current (NAC) supplying water towards the eastern SPNA.

315 | Two branches of the NAC are evident (**Figure 3a**): the majority of the floats (~~not shown~~) drift far eastward in a
strongly meandering current band ([300-350 km wavelength](#)) until arriving at the topography (still at the latitude
of the CGFZ, i.e., 52°N). Thereafter the flow follows the topography northward into the Rockall Trough west of
Ireland. On the western flank of the Rockall Plateau a narrow eastern boundary current forms and flows
northward until it reaches the Iceland-Scotland-Ridge, where it feeds the southwestward boundary current
(discussed above) that eventually becomes a 'western' ~~Boundary~~Boundary Current along the Reykjanes ridge.
320 | However, the broadest inflow comes from the mid-basin flow regime extends from the NAC northward from
about 27°W, and follows the deep trench northward to 62°N. This mid-basin flow is characterized by stable
advection and several large wavenumber meanders.

3.1.5 The North Atlantic Current regime

325 | The southern exit of the Labrador Sea is the region where the NAC meets the DWBC (**Figure 5a**), and while the
LSW follows the topography inside a topographic feature called 'Orphan Knoll' (50°N, 46°W), the NAC is
located seaward of 'Orphan Knoll' and retroreflects toward east in a feature known as the 'Northwest Corner'
(NWC). The latitude of the NWC is also at 52°N, and from there the NAC meanders eastward through the
CGFZ. The zonal flow field and the associated southern signature of the Polar Front can be interpreted as the
southern limit of the SPNA and it forms the zonal component of the large scale cyclonic circulation. In the LSW
330 | depth range the Polar-Front separates the lighter water to the south from the denser subpolar gyre.

3.2 Gridded Mean Flow

By application of the GI-method, the velocity field was interpolated to a regular grid of 0.25° latitude and 0.5° longitude (Figure 5a). As for the raw data maps (Figure 3a) the gridded data reflects all the major circulation elements. The interpolation method keeps the deep ~~Boundary~~boundary currents as narrow- and stable jets which are resolved by five or more grid points. Mid basin jets in the Irminger Sea and the Iceland Basin appear as continuous but meandering pathways of the intermediate deep circulation. The correspondence of the current field and the potential density at 1500m depth is evident. The strongest density gradients are associated with the western boundary current elements along the eastern Reykjanes Ridge, associated with the EGC, and to a lesser extent with the Deep Labrador Current (DLC). In combination with the deep density the major export routes for newly ventilated LSW are also visible in the potential density pool of the central Labrador Sea draining into the Irminger Sea. There is also a connection between the NWC and the convection area by a low density anomaly that is not associated with the DWBC, but with the reverse circulation into the Labrador Sea.

Although, we only show the mean gridded flow field from the GI-method we do obtain the same results from the OI method. The differences of the two estimations mainly contain small scale elements that reflect the scales of the influence radii by either method.

3.3 Gridded Eddy Kinetic Energy

From the individual u' and v' fields we generated a smoothed and gridded version of the EKE (Figure 5b) using the same interpolation parameters as for the mean field – i.e., both fields have the same length scales in consideration, and the grid is identical. ‘Smoothed’ also means that some de-spiking and noise reduction during the gridding operation was applied, as there were a few individual spikes along the edges of the mapping environment, i.e. in regions where the mapping area intersects the 1500m topography and where floats might have become bottom-stuck. These spikes could be easily detected and accounted to less than 2% of the data contributing to an individual grid point. As a result the cleaned EKE distribution is smoother and more reliable.

We note several intense EKE hot spots in the Labrador Sea, in the ‘Northwest Corner’ of the North Atlantic Current, and in the eastern SPNA located east and west of the Rockall-Plateau. While it is not surprising that the retroflexion of the NAC (i.e. the ‘Northwest Corner’) shows large EKE values exceeding $250 \text{ cm}^2 \text{ s}^{-2}$, it is surprising that the zonal basin-crossing of the NAC has relatively weak EKE at LSW levels. The second strongest EKE is located in the northeastern Labrador Sea and is generated by instabilities and eddy shedding of the West Greenland Current (WGC), known to occur from surface flow observations. This EKE maximum shows relatively large values around $60 \text{ cm}^2 \text{ s}^{-2}$ and covers a large fraction of the interior Labrador Sea. Then there are mid-basin EKE maxima in both the Irminger Sea and even stronger in the Iceland Basin, extending along the whole lengths of the basins. Interestingly, there are EKE minima along both sides of the Reykjanes ridge and zonally all across the basin just north of the NAC. Comparably weak EKE is located directly at the topography off Labrador and off East Greenland where the DWBC is stabilized by the steep topography.

The EKE maximum in the central Labrador Sea has been linked in the past to the West Greenland Current (WGC) (e.g. Brandt et al. 2004, Eden and Böning, 2002). For example Eden and Böning (2002) attributed the

EKE maximum to barotropic instability of the WGC with a seasonal peak at the time of maximum surface forcing (winter wind-stress maximum). It appears that there is a significant difference of the EKE intensity on both sides of the Labrador Sea; while the northward flowing WGC is subject to intense eddy formation and hence high EKE, the southward flowing Deep Labrador Current is much more stable with remarkably low EKE levels. A possible reason is the PV-conservation that stabilizes the flow when progressing southward (towards lower f) and consequently the flow is driven toward the stabilizing topography, while for northward flow there is a tendency to move into deeper water with smaller topographic ~~beta~~ beta or less cross-flow topographic slope. This is further supported by the weak EKE in the southward flowing East Greenland Current.

3.4 Advection versus Diffusion -- Peclet Number

The western subpolar basin has very different regimes regarding mean flow and EKE pattern. Even at larger greater depths, there are narrow boundary currents along the topography, ~~there are~~ interior persistent current bands, and ~~there are~~ regimes of almost stagnant mean flow with intense eddy motion, but it is a priori not clear which of the processes – advection or diffusion dominates in either of the circulation regimes. This objective is investigated through the calculation of a local dimensionless number, the Peclet Number (Pe), which is the ratio of advection to diffusion. Here, we calculate a simplistic Pe-version that allows to regionally compare the the relative importance of advection versus diffusion:

$$Pe = L_d * \langle U \rangle / K; \text{ with } K = \alpha \sqrt{EKE} * L_d ; \quad \text{for EKE see Figures 3b, 6a;}$$

α is an empirical (non physical) scaling factor; here we chose $\alpha = 0.25$, such that the resulting Pe -field varies between zero and one; L_d = Lagrangian length scale chosen to be related to the first baroclinic Rossby Radius (order 1 to $2 * 10^4$ m); $\langle U \rangle$ = is the mean current speed taken from the gridded velocity fields.

The resulting Pe -distribution (**Figure 5c**) basically shows two regimes; one with very small Pe (i.e. $Pe < 0.2$), and these are the regions where the deep eddy motion is a strong component of dominates the current field, such as the central basins of the SPNA with the central Labrador Sea being the largest area with low Pe . Similarly, the southern Irminger Sea shows low values of Pe , and in addition to these, the transatlantic zone south of the CGFZ is also subject to intense eddy motion.

The contrasting regimes with strong mean flow and relatively high Pe are the Boundaryboundary C currents along the east- and west Greenland shelves and all along the Labrador coastline. There are also deep western and eastern boundary currents along the Reykjanes Ridge and along the Rockall Plateau. In these areas, the advection is relatively strong compared to the eddying motion. Finally, there are mid-basin regions with stable advection and relatively weak eddy motions away from the topography and associated with the cyclonic recirculation cells. One such regime is south of Cape Farewell and it extends far into the Irminger Sea; this band connects the ‘convection regime’ of the central Labrador Sea with the central Irminger Sea. A similar mid-basin advection regime is found in the Iceland Basin where it connects the high Pe -band associated with the zonally oriented Polar Front at $52^\circ N$ with the meridional current band directed along the deep Maury Channel, i.e. the central axis of the Iceland Basin. Finally, the recirculation regime off the Labrador shelf break is associated with relatively high Pe , as the eddy motion is relatively weak.

Formatiert: Schriftartfarbe:
Automatisch

405 **4 Verifications of the results**

We verified our results in three different ways: First the results from GI and OI were compared in order to identify a superior interpolation method. Then we compared the mean flow and mean EKE fields with similar quantities derived from Eulerian time series data from moored stations (EKE_{moor}) in the region; and the third way of verification was a comparison between the deep EKE and the EKE_{surf} from satellite SLA data.

410

4.1 Consistency of interpolation techniques

The mean flow fields from the two gridding methods are surprisingly similar and there are no significant differences between the velocity and speed fields. The overall speed-difference is -0.16 cm s^{-1} which illustrates that there are no systematic differences (biases) between the two speed estimates as a result of the gridding technique. The difference field ~~are is~~ patchy in structure with patch-scales of the order of the interpolation radii. Thus, by choosing the GI method, the current map (Figure 5a) is considered representative and independent of the two mapping procedures applied.

415

Likewise the difference in GI and OI interpolated EKE fields (Figure 6) agreed well. Most of the EKE differences occurred in the range $\pm 5 \text{ cm}^2 \text{ s}^{-2}$ with the strongest deviations around the NAC path across the SPNA – here, the GI method produces somewhat larger values. In contrast, the Northwest Corner reveals larger EKE values for the OI method. A patchy structure is observed with scales associated to the influence radii of the gridding methods (roughly 100km). The difference has an overall Gaussian distribution but with a slight bias of $1 \text{ cm}^2 \text{ s}^{-2}$ toward larger EKE in the OI method map. ~~The magnitude of this bias depends on de-spiking method used in any of the two processing methods. We note that each of the mapping procedures requires despiking of the velocities (see e.g. spikes in the eddy field near the boundary, Figure 3), which is treated differently in the two methods..~~ The strongest impact ~~on the EKE field~~ is due to the removal of individual large ~~velocity spikes in the EKE~~ in the GI method, which leads to a regional reduction of the corresponding EKE field. ~~In this procedure we sorted the selected eddy velocity data (typically within the cut-off scales – order 100km – about 100-200 data points) with respect to their magnitude, and removed the largest of the data. Removing only the 1% largest eddy velocities results in a positive bias of~~ ~~The removal of only 1% of the largest velocities results in an increased in bias to~~ $4 \text{ cm}^2 \text{ s}^{-2}$; ~~When using additional statistical criteria, e.g. removal of data only if exceeding a threshold based on statistics (like two times the standard deviation) then the bias would be in the range 1 to 2~~ $\text{cm}^2 \text{ s}^{-2}$. This might be taken as a cautionary hint for interpreting the EKE map as a quantitative measure for the ~~small scale details of the eddy field.~~ ~~No explicit de-spiking has to be used in the OI method, as it is inherent in the method itself (see Schmidtko et al., 2013), while in the GI method we explicitly had to remove some large outliers.~~

420

425

430

435

Kommentar [JF1]: See OI method description

4.2 Comparison with local Eulerian measurements

The second method for verification was a comparison between the derived mean fields ($\langle U \rangle$ and EKE) and selected locations where time series data from moored instrumentation was available (Figure 5b; table 1).

440

4.2.1 Labrador- and Irminger Seas

445 In the ²convection² area of the Labrador Sea a time series of currents is available at the K1 site since 1996 (the site is close to where the Ocean Weather Ship ²Bravo²(56°30'N, 51°00'W) was operated). The mooring had
continuous velocity records at 1500 m depth (from 1996 to 2016) and a shorter record at 750m (from 2006 to
450 2016) (Figure 7). In general the mean flow at the location of K1 is very weak (order 1cm/s) with a
northwestward direction into the Labrador Sea and, given the mooring position, consistent with the anticyclonic
circulation around the basin center (Figure 5a). Short time scales dominate the variability of the flow (Figure 7),
and the spectra indicate that the bulk of the energy is on intra-seasonal periods with strong decay toward longer
455 time scales. The strongest variations occur in late spring and are associated with eddies shed by the WGC near
the location of Cape Desolation (Avsic et al. 2006; Funk et al., 2009). These eddies are only weakly sheared in
the LSW depth range which is an important aspect as it supports combining 1000 m and 1500 m parking depths
Argo float displacements. The EKE from 180d high pass filtered time series is around $170 \text{ cm}^2 \text{ s}^{-2}$ in both levels,
750m and 1500m (Table 1). These values are larger than what is derived from the Argo data set and we interpret
460 this to be a result of the inherent low pass filter in the float processing. With respect to the Pe (Figure 5c) the
area is characterized as an eddy dominated regime.

In the central Irminger Sea (CIS) a current time series is available at about 1000 m depth. As for K1, the site is
characterized by a weak mean flow (around 1 cm s^{-1}) while the EKE (based on intra seasonal velocity
fluctuations) is around $80 \text{ cm}^2 \text{ s}^{-2}$ (Fan et al. 2013). The location of CIS is at the edge of the mid-basin velocity
465 band connecting the Labrador Sea around the tip of Greenland, and into the Irminger Sea.

In the boundary current system of the Labrador Sea a number of records could be analyzed. In general the flow is
rather stable and strong (Lazier and Wright, 1993; Fischer et al., 2004); ~~see (compare~~ also Table 1).
Representative for the DWBC at 53°N (K9, Zantopp et al., 2017) the long term mean flow along the topography
is 12.5 cm s^{-1} and the EKE (again for periods less than 180d) is $62 \text{ cm}^2 \text{ s}^{-2}$. Farther toward the topography the
470 mean speed is even larger and the EKE smaller, as the DWBC appears to be more focused by the steep
topography at 53°N. In any of the boundary current records a large energy contribution is on timescales less than
10 to 20 days (Fischer et al., 2015), which are not captured by the Argo displacement vectors and different from
the basin interior where the flow variability is on timescales longer than a month and thus better resolved by 10
day displacement vectors from Argo (Figure 8).

475 In the records in the center of the DWBC at Hamilton Bank the total EKE of the moored record is larger than
that from the float displacement but similar to K9 (Table 1). For a better comparison we calculated the EKE
fraction that Argo would represent in their 10 day displacement vectors by low-pass filtering the mooring data
(10d cut-off period of the filter). Then, the EKE values coincide much better as is demonstrated by the colored
mooring numbers in Figure 5b.

Near the offshore edge of the DWBC, at mooring K10 of the 53°N array, the flow speed is rather low, as the
mooring lies in the transition regime between the DWBC and the recirculation pathway in the upper 2000 m,

Formatiert: Schriftart: (Standard)
Times New Roman, 10 Pt., Englisch
(USA)

480 while at deeper depths it is still part of the DWBC (Zantopp et al., 2017). At 1500 m the flow is mainly reverse
to the DWBC direction and the EKE is rather small, but in good agreement with the EKE from Argo.

Associated with weak mean speeds (only 10% of the DWBC speed is found at locations offshore of K10) and
moderate EKE_{moor} values coincide when the resulting Peclet Numbers (**Figure 5c; Table 1**) are low and indicate
sufficient diffusion in the presence of weak advection. This structure is reflected in the Argo flow pattern, which
485 shows an increasing advective contribution further toward the basin interior, and from the mean current map and
the density field it is tempting to assume this route as one of the supply routes for the deep central Labrador Sea.

490 4.2.2 Subpolar Locations

Moored observations in the Iceland-Scotland-Overflow Water were available at 4 positions (Named I, S, O, W;
see Kanzow and Zenk, 2014). Only three (S, O, W) moorings delivered data in the appropriate depth range for
this study. While S was located in the area of low deep EKE, the fluctuations increase toward east with mooring
W located in the EKE max along the northward flow (**Figure 5a**).

495 North of the I S O W array the **Iceland Array** is located at the shelf break south of Iceland, and the northern
mooring direct at the topography reflects the low EKE_{moor} typical for topographically guided currents, while the
one further offshore is located in the northern extension of the EKE maximum of the Iceland Basin.

During the Jasin program in the late 1970s a number of moorings were deployed in the northern Rockall Trough
(Gould et al., (1982)) and these moorings reflect the intermediate intensity of the deep EKE_{moor} that is also
500 present in the Argo derived values (**Table 1**).

The EKE from the moorings represent mean regional variations. In order to compare the high resolution time
series with the Argo data a 10d low-pass filter is applied. There is a remaining discrepancy between EKE from
Argo and from moorings with a tendency that in region with low EKE (taking now the Argo derived map as a
505 reference) the Argo estimates are larger than the 10d-lowpass filtered mooring estimates, while in regions of
high EKE the situation is reversed. We interpret this discrepancy by the inherent (nonlinear) temporal filtering in
the EKE derived from Argo that tend to low-pass filter the field with an unpredictable filter characteristics
(depending at which times the floats enter the corresponding interpolation radius).

510 4.3 Surface EKE versus intermediate depth EKE

In addition to the deep EKE we estimated the surface EKE (EKE_{surf}) field calculated from remote sensing-based
ADT observations. The geostrophic surface flow from SLA contains variability over a wide range of
frequencies, and some of the long term components are not generally thought to be part of the turbulent eddy
515 field. Thus, we extracted the intra-seasonal variability by applying a high-pass filter (Hanning window) with a
cut-off period at 180d. The result is a field of geostrophic fluctuations from which we calculate EKE_{surf} (**Figure
8a**). This field is independently derived, and thus allows an independent comparison of the Argo-derived fields
(here, the deep circulation and EKE).

520 The EKE_{surf} also resembles major (deep) circulation elements, such that the zonal flow in the CGFZ region
located underneath the zone of maximum EKE_{surf} gradient at the surface. (Note in Figure 8 only currents larger
than 1.5cm s^{-1} are shown and thus, only vector magnitudes that would be sufficient to travel one Rossby Radius
within the 10 d schedule of the floats are included). A similar surface versus deep EKE and flow pattern is seen
for the northeastern flow from the Labrador Sea into the Irminger Sea. Within the Iceland Basin the deep flow is
525 associated with the surface EKE_{surf} maximum, suggesting the mid basin path is present from surface to LSW
depth range. Interestingly the surface EKE shows a clear EKE minimum all along the DWBC in the western
SPNA, and this is due to the slanting shape of the ~~Boundary~~Boundary circulation and the slope of the western
shelves. In a region with less slope, i.e. the northern Labrador Sea we observe strong EKE at all levels (surface
and LSW depth range). This is the area, when the deep WGC turns away from the steep Greenlandic shelf and
intense eddies are formed and shed from the DWBC (Eden and Böning 2002).

530 Following Ollitrait and de Verdiere (2013) we calculated the logarithmic ratio of surface EKE to the deep EKE;
i.e. $\ln(EKE_{surf} / EKE)$, such that the ratio becomes negative when the deep EKE is larger than that at the
surface. Generally, in a baroclinic ocean one would expect positive ratios, with the EKE_{surf} sufficiently larger
than the EKE at depth, as is the case for the region south of the North Atlantic Drift, i.e., south of 52°N . A global
much coarser map of such a ratio reveals that this is the case for almost the whole Atlantic Ocean (Ollitrait and
535 de Verdiere; 2013). In their paper, the subpolar North Atlantic appears as broad negative area in which the deep
EKE exceeds the upper layer or is of similar magnitude. The much higher resolution of the field generated herein
(Figure 8b), allows a more detailed view, which reveals two centers of deep EKE dominance. The first is
associated with the DWBC all along the Labrador shelf break and the strongest signal around Hamilton Bank.
The second center is associated with the deep action center south of Cape Farewell that shows both, stable
540 advection and EKE at depth, while at the surface these components are rather weak. This zone extends far north
into the Irminger Sea where it appears to be related to the deep EGC and its variability. This behavior indicates
that for the interbasin spreading and mixing of newly formed water masses the deep EKE field contains
important information, which is not easily available elsewhere; at least not from the surface variability alone.

Besides the boundary current related anomalies there is one additional zone in which the deep EKE is close to
545 the surface EKE, and that is along the CGFZ at the northern flank of the NAC. In this area the flow is guided by
the deep topography and advection appears to be dominating the zonal flow (relatively large Pe).

5 Summary and Conclusion

The results of the investigation can be summarized as follows:

- 550
- 1) Based on nearly 17 years of quality controlled Argo displacement vectors a high resolution ($\sim 25\text{km}$ grid) map of mean flow in the depth layer of the LSW was constructed for the Subpolar North Atlantic. Robust circulation elements were identified consisting of boundary currents along topographic slopes, mid-basin advective pathways, and stagnation regimes with very low mean speeds.

- 555 2) The mapping procedures were twofold: Gaussian Interpolation (GI) and Optimum Interpolation (OI), both methods were applied using potential vorticity constraints, and the resulting mean flow fields were very similar – almost identical.
- 560 3) The second product was the fluctuating (eddy -- u' , v') velocity component, which was determined as the residual after subtracting the average and potential vorticity conserving contribution from the individual measurements (displacement vectors). The u' , v' -fields were used to map the mean EKE-distribution; to our knowledge for the first time.
- 565 4) The ratio of mapped mean flow to the square root of the EKE, the Peclet-Number (Pe), was estimated and showed regions that are advection dominated (boundary currents and internal LSW routes), and regions with low PE, in which eddy diffusion prevails.
- 570 5) The mapped fields were analyzed for consistency between the OI and GI method. In addition velocity time series from moored sensors were used to estimate mean flow and EKE in an attempt to verify the mapped fields locally with independent data. While the general pattern of high and low EKE regimes are consistent, but the mooring EKE appears to be larger than EKE from Argo but the differences become smaller, when the Eulerian measurements are lowpass filtered with a cut-off at the Argo sampling time scale (10d).
- 575 6) Comparing the mid depth EKE with the independently derived surface EKE from Aviso SLA-data, we found qualitative agreement of the two fields in many regions, with the surface EKE larger than the mid depth EKE. However, other regions showed the local EKE maxima were horizontally displaced between surface and the deep EKE, thus there are areas with ~~and with~~ larger EKE at mid depth. This seems to be a special (robust) feature of the subpolar North Atlantic.

The gridded velocity field can be used for a variety of follow up investigations, e.g. estimating water mass spreading via artificial tracer release experiments or using the gridded flow field as a reference level velocity for geostrophic calculations (e.g. based on Argo derived geostrophic shear).

580 By focusing on the Labrador Sea, the “surprisingly rapid spreading” of LSW throughout the subpolar North Atlantic (Sy et al., 1997) is well supported by our gridded mean flow field: newly formed LSW is exported by the mid-basin advective pathway into the Irminger Sea (**Figures 3a and 5a**) and eastward through the pathway that connects the western SPNA with the northern Iceland Basin through the NAC and its northern pathway. Individual floats released in the DWBC off Labrador used that path to drift within a few (3-4) years far north

585 into the Iceland Basin.

More regional aspects were discussed in the float release experiments performed in the late 1990, i.e. before Argo started officially. On the basis of these investigations, export pathways for LSW out of the Labrador Sea were discussed (e.g. Straneo et al., 2003) in which the export of LSW into the Irminger Sea, and the ~~b~~Boundary ~~b~~Current ~~b~~Export around Flemish Cap were identified as major export routes. While the Irminger Sea route appears strong and robust, the flow along the topography (Flemish Cap ~~and Grand Banks~~) is relatively narrow and the EKE maximum in this region is due to the NAC interaction with the upper part of the DWBC near the steep topographic slope. Another weak. Instead, the second major export route is into the eastern SPNA via the NAC pathroute along 52°N.

590

595 Traditionally the upper ocean eddy variability represented by the EKE distribution has been investigated from
SLA data (Brandt et al., 2004, Funk et al. 2009). Just recently (Zhang and Yan, 2018) the Labrador Sea surface
EKE based on altimeter data has been investigated with regard to interannual to decadal variability in the time
period 1993 to 2012. They find strong interannual variability in the EKE field near the WGC, but no trend over
the observational period.

600 Generally, mid depth EKE maps based on observational data are rare but important for the deep ocean water
mass and tracer spreading. Thus, both the mean current field and the EKE at the transition between the deep
water masses LSW to LNADW should be useful metrics for ocean model evaluations.

6 Data availability

605 The raw data is available through open access from: YoMmaHha'07
(<http://apdrc.soest.hawaii.edu/projects/yomaha/index.php>). Aviso (<http://marine.copernicus.eu/services-portfolio/access-to-products/>), Coriolis Data center (<http://www.coriolis.eu.org/>). The data products derived
herein will be made freely available with the publication. The data set will contain gridded (latitude/longitude
grid) versions of velocities and eddy kinetic energies alongside with water depth at grid location.

610 **Author contribution:** Jürgen Fischer prepared the manuscript with contributions from all co-authors, all authors
worked on the analysis of the data: Johannes Karstensen in general and on moored records; Marilena Oltmanns
on Argo profile data, and Sunke Schmidtke applied the OI method.

615 **Acknowledgements:** This project has received funding from the European Union's Horizon 2020 research and
innovation program under grant agreement 63321 (AtlantOS) and grant agreement 727852 (Blue-Action). The
Argo data were collected and made freely available by the international Argo project and the national programs
that contribute to it (<http://doi.org/10.17882/42182>). We further acknowledge the YoMmaHha'07 group for
generating the Argo displacement data set. This paper contains products from data supplied by Natural
Environment Research Council, and from data gathered by the RACE program of the German Ministry BMBF.
OOI data were obtained from the NSF Ocean Observatories Initiative Data Portal,
<http://ooinet.oceanobservatories.org>. Mooring metadata is available via BODC and the OceanSITES network
620 (www.oceansites.org).

Feldfunktion geändert

References

- Avsic, T., Karstensen, J., Send, U. and Fischer, J. (2006) Interannual variability of newly formed Labrador Sea
Water from 1994 to 2005. *Geophysical Research Letters*, 33 (L21S02). DOI 10.1029/2006GL026913.
- 625 Bower, A. S., M. S. Lozier, S. F. Gary, and C. W. Böning,(2009), Interior pathways of the North Atlantic
meridional overturning circulation, *Nature*, Vol 459, doi:10.1038/nature07979

- Brandt, P., Schott, F., Funk, A. und Sena Martins, C. (2004) Seasonal to interannual variability of the eddy field in the Labrador Sea from satellite altimetry. *Journal of Geophysical Research - Oceans*, 109 . C02028. DOI 10.1029/2002JC001551.
- 630 Chelton, D. B., R. A. deSzoeke, and M. G. Schlax, K. El Naggar, and N. Siwertz (1998), Geographical Variability of the First Baroclinic Rossby Radius of Deformation, *J. Phys. Oceanogr.* Vol 28, pp 433-460, [https://doi.org/10.1175/1520-0485\(1998\)028<0433:GVOTFB>2.0.CO;2](https://doi.org/10.1175/1520-0485(1998)028<0433:GVOTFB>2.0.CO;2)
- Daniault, N., H. Mercier, P. Lherminier, A. Sarafanov, A. Falina, P. Zunino, F. F. Pérez, A. F. Ríos, B. Ferron, T. Huck, V. Thierry, and S. Gladyshev; (2016), The northern North Atlantic Ocean mean circulation in the early 21st century. *Progress in Oceanography* 146, 142–158
- 635 Davis, R. E., 1998: Preliminary results from directly measuring mid-depth circulation in the tropical and South Pacific. *J. Geophys. Res.*, 103, 24 619–24 639.
- Davis, RE, Sherman JT, Dufour J. 2001. Profiling ALACEs and other advances in autonomous subsurface floats. *Journal of Atmospheric and Oceanic Technology.* 18:982-993. 10.1175/1520-0426(2001)018<0982:paoai>2.0.co;2
- 640 Davis, R.E., 2005: Intermediate-Depth Circulation of the Indian and South Pacific Oceans Measured by Autonomous Floats. *J. Phys. Oceanogr.*, 35, 683–707, <https://doi.org/10.1175/JPO2702.1>
- Eden, C., Böning, C., (2002); Sources of eddy kinetic energy in the Labrador Sea. *Journal of Physical Oceanography*, 32 (12), pp. 3346-3363. DOI: 10.1175/1520-0485(2002)032<3346
- 645 Fan, X., Send, U., Testor, P., Karstensen, J. and Lherminier, P. (2013) Observations of Irminger Sea Anticyclonic Eddies. *Journal of Physical Oceanography*, 43 (4). pp. 805-823. DOI 10.1175/JPO-D-11-0155.1.
- Fischer, J. and Schott, F. (2002) Labrador Sea Water tracked by profiling floats - from the boundary current into the open North Atlantic *Journal of Physical Oceanography*, 32 . pp. 573-584. DOI 10.1175/1520-0485(2002)032
- Fischer, J., F. Schott, and M. Dengler (2004), Boundary circulation at the exit of the Labrador Sea, *J. Phys. Oceanogr.*, 34, 1548–1570.
- 650 Fischer, J., Karstensen, J., Zantopp, R. J., Visbeck, M., Biastoch, A., Behrens, E., Böning, C. W., Quadfasel, D., Jochumsen, K., Valdimarsson, H., Jónsson, S., Bacon, S., Holliday, N. P., Dye, S., Rhein, M. und Mertens, C. (2015) Intra-seasonal variability of the DWBC in the western subpolar North Atlantic. *Progress in Oceanography*, 132 . pp. 233-249. DOI 10.1016/j.pocean.2014.04.002.
- 655 Funk, A., P. Brandt, and T. Fischer (2009) Eddy diffusivities estimated from observations in the Labrador Sea; *J. Geophys. Res.* , Vol. 114, C04001, doi:10.1029/2008JC005098
- Gould, WJ, A. Cutler, and D. Weddell (1982) Long-term current measurements in the N. Rockall Trough, Summer 1978 to Autumn 1980. (Department of Energy Contract No.OT/F 497).

Feldfunktion geändert

660 Griffies et al. (2016), OMIP contribution to CMIP6: experimental and diagnostic protocol for the physical component of the Ocean Model Intercomparison Project, *Geosci. Model Dev.*, 9, 3231–3296, doi:10.5194/gmd-9-3231-2016

Kanzow, T. and , W. Zenk (2014); Structure and transport of the Iceland Scotland Overflow plume along the Reykjanes Ridge in the Iceland Basin; *Deep-Sea Research I* 86(2014) 82–93;

LaCasce, J.H., (2000): Floats and f/H; *Journal of Marine Research*, 58, 61–95, 2000

Lavender, K. L., Davis, R. E. & Owens, W. B. Mid-depth recirculation observed in the interior Labrador and Irminger seas by direct velocity measurements. *Nature* 407, 66–69 (2000).

670 Lavender, K. L., W. B. Owens, and R. E. Davis, 2005: The middepth circulation of the subpolar North Atlantic Ocean as measured by subsurface floats. *Deep-Sea Res. I*, 52, 767–785, doi:10.1016/j.dsr.2004.12.007.

675 [Lazier, J. R. N., and D. G. Wright, 1993: Annual velocity variations in the Labrador Current. *J. Phys. Oceanogr.*, 23, 559–678.](#)

Formatiert: Englisch (USA)

Formatiert: Englisch (USA)

680 [Lebedev, K.V. H. Yoshinari, N. A. Maximenko, and P. W. Hacker, 2007: YoMaHa'07: Velocity data assessed from trajectories of Argo floats at parking level and at the sea surface. *IPRC Technical Note No. 4\(2\), June 12, 2007.*](#)

Formatiert: Schriftart: Nicht Fett, Englisch (USA)

Formatiert: Schriftart: Nicht Fett

Formatiert: Schriftart: Nicht Fett, Englisch (USA)

Le Traon, P. Y., F. Nadal, and N. Ducet. An improved mapping method of multisatellite altimeter data. *Journal of atmospheric and oceanic technology*, 15(2):522–534, 1998.

685 National Geophysical Data Center, 2006: 2-minute Gridded Global Relief Data (ETOPO2) v2. National Geophysical Data Center, NOAA. doi:10.7289/V5J11012Q.

690 [Lozier, M. S. Bacon, S., Bower, A. S., Cunningham, S. A. de Jong, M. F., de Steur, L., deYoung, B., Fischer, J., Gary, S. F., Greenan, B. J.W., Heimbach, P., Holliday, N. P., Houpert, L., Inall, M.E., Johns, W. E., Johnson, H. L., Karstensen, J., Li, Feili; Lin, X., Mackay, N., Marshall, D. P., Mercier, H., Myers, P. G., Pickart, R. S., Pillar, H. R. Straneo, F., Thierry, V., Weller, R. A., Williams, R. G., Wilson, C., Yang, J., Zhao, J., Zika, J. D., 2016 *Overturning in the Subpolar North Atlantic Program: a new international ocean observing system. Bulletin of the American Meteorological Society*, 10.1175/BAMS-D-16-0057.](#)

695 Ollitraut, M. and Colin de Verdiere; The Ocean General Circulation near 1000-m Depth, (2013), *J. Phys. Oceanogr.*, 44, 384–409, DOI: 10.1175/JPO-D-13-030.

Palter, J. B., C.-A. Caron, K. L. Law, J. K. Willis, D. S. Trossman, I. M. Yashayaev, and D. Gilbert (2016), Variability of the directly observed, middepth subpolar North Atlantic circulation, *Geophys. Res. Lett.*, 42, doi:10.1002/2015GL067235.

700 Pickart, R., F. Straneo , and G. Moore (2003), Is Labrador Sea Water formed in the Irminger Basin? Deep Sea Research I 50, 23–52.

[Schmidtko, S., Johnson, G. C. und Lyman, J. M. \(2013\) MIMOC: A global monthly isopycnal upper-ocean climatology with mixed layers. Journal of Geophysical Research-Oceans, 118 \(4\). pp. 1658-1672. DOI 10.1002/jgrc.20122](#)

705 [Schott, F., Stramma, L., Zantopp, R. J., Dengler, M., Fischer, J. und Wibaux, M. \(2004\) Circulation and deep water export at the western exit of the subpolar North Atlantic. Journal of Physical Oceanography, 34 . pp. 817-843. DOI 10.1175/1520-0485\(2004\)034<0817:CADEAT>2.0.CO;2](#)

[Spall, M. A., and R. S. Pickart, 2003. Wind-driven recirculations and exchange in the Labrador and Irminger Seas. Journal of Physical Oceanography, 33, 1829—1845.](#)

710 Straneo, F., R. S. Pickart, K. Lavender, (2003), Spreading of Labrador sea water: an advective-diffusive study based on Lagrangian data, Deep-Sea Research I 50, 701–719.

Sy, A., Rhein, M., Lazier, J.R.N., Koltermann, K.P., Meincke, J., Outzka, A., Bersch, M., (1997), Surprisingly rapid spreading of newly formed intermediate waters across the North Atlantic Ocean. Nature 386, 675–679.

715 Yoshinari, H., N. A. Maximenko, and P. W. Hacker, 2006: YoMaHa'05—Velocity data assessed from trajectories of Argo floats at parking level and at the sea surface. IPRC Tech. Note 4, 16 pp.

Zantopp, R., J. Fischer, M. Visbeck, and J. Karstensen (2017), From interannual to decadal: 17 years of boundary current transports at the exit of the Labrador Sea, J. Geophys. Res. Oceans, 122, doi:10.1002/2016JC012271.

Zhang, W., & Yan, X.-H. (2018); Variability of the Labrador Sea surface eddy kinetic energy observed by altimeter from 1993 to 2012. Journal of Geophysical Research: Oceans, 123. <https://doi.org/10.1002/2017JC013508>

725

730

Formatiert: Englisch (USA)

Feldfunktion geändert

Formatiert: Englisch (USA)

Formatiert: Englisch (USA)

Feldfunktion geändert

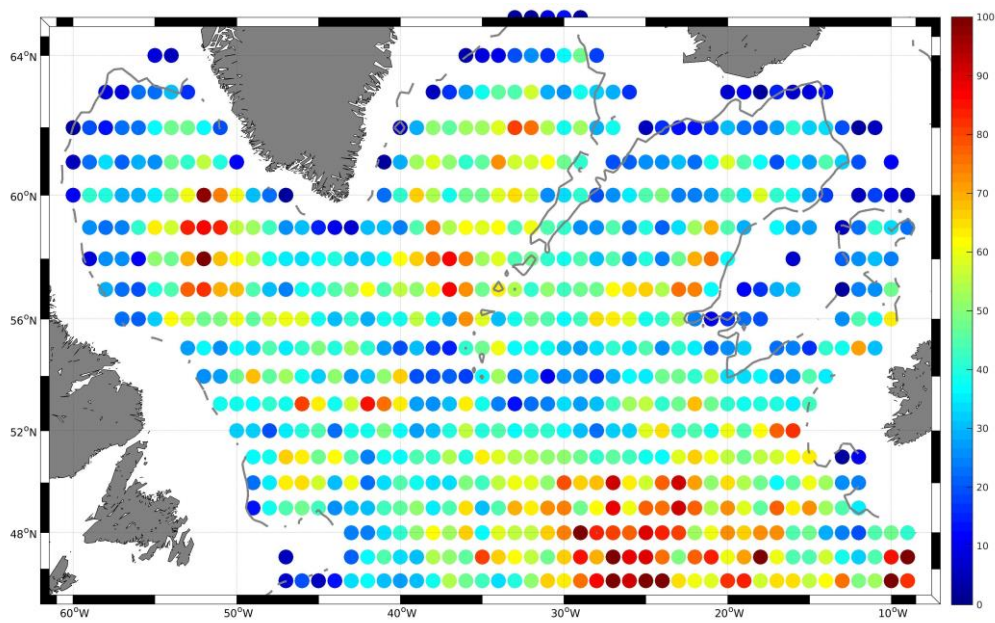
Formatiert: Englisch (USA)

Formatiert: Englisch (USA)

735

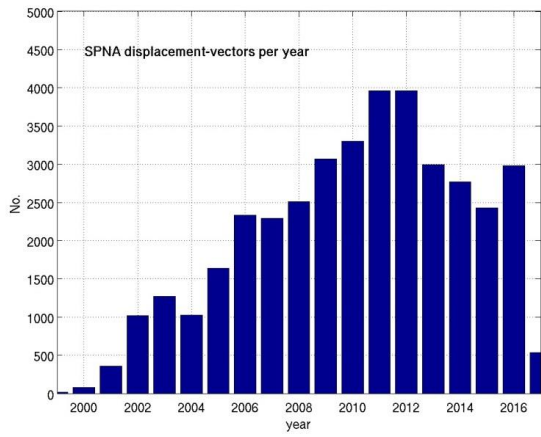
740

Figures



745

Figure 1: Data density in $1^{\circ} \times 1^{\circ}$ fields; the number of 10d- displacement vectors per cell.



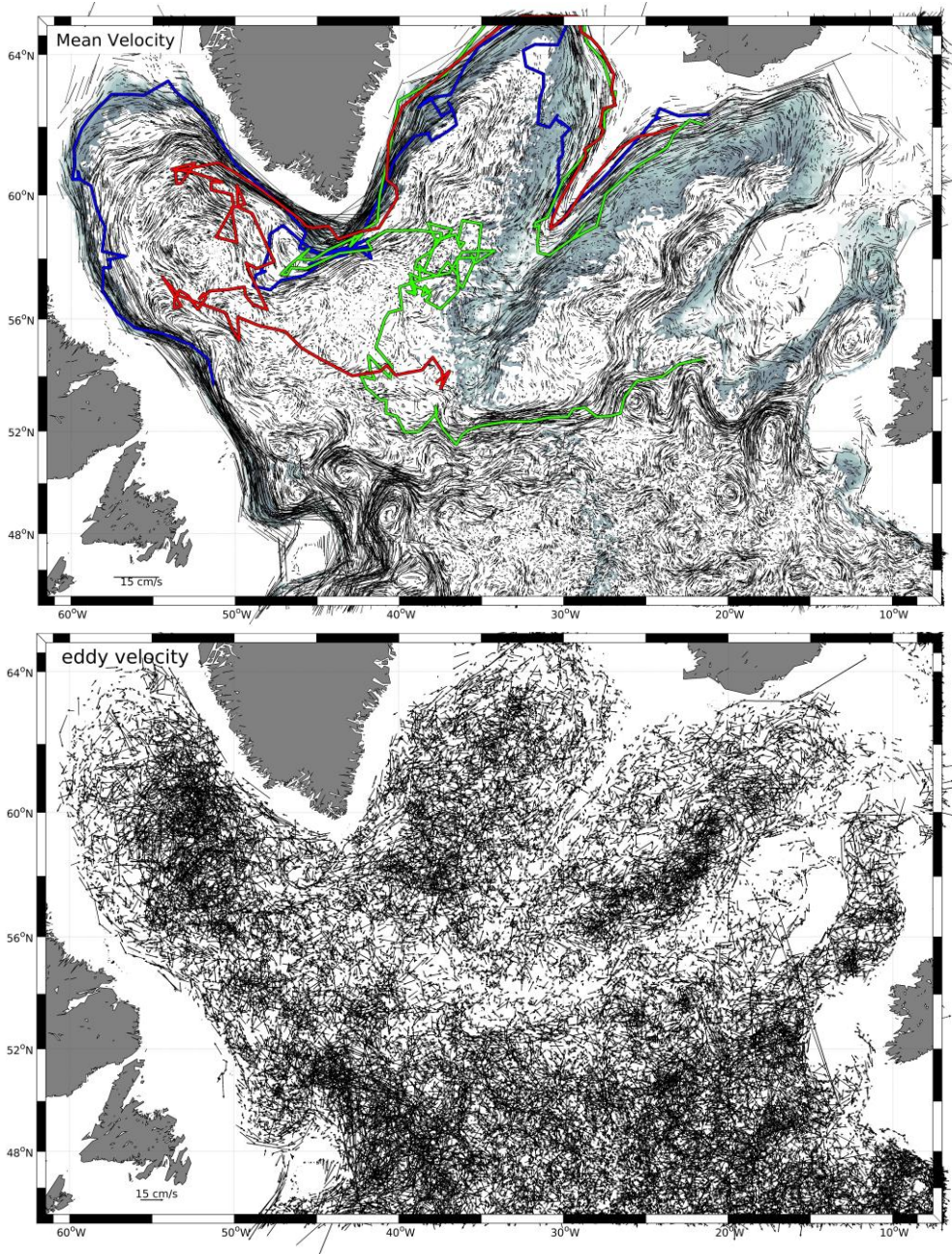
750

Figure 2: Temporal evolution of the Argo data density in the subpolar domain independent of the parking depth (1000 m and 1500 m), and from year 2000 to March 2017.

755

760

765



770 | **Figure 3: Mid-depth circulation (a) in the western subpolar NA from ~38500 Argo deep drifts (1000m or 1500m parking depth) derived from the YoMmaHha'07 data. This is an attempt to present the advective contribution of the flow field at each measurement location; i.e. for each measured 10-day drift vector (for details of the processing see text). Colored lines for selected float trajectories (deployed in the Iceland basin); bluegrey shaded area is for the topographic depth range (1500m to 2500m). The residual (b) is thought to be u',v' , the eddy velocity contribution to the flow field. — note, the scaling vector in (b) is a factor 2 larger than in 3a.**

775 |

780

785

790

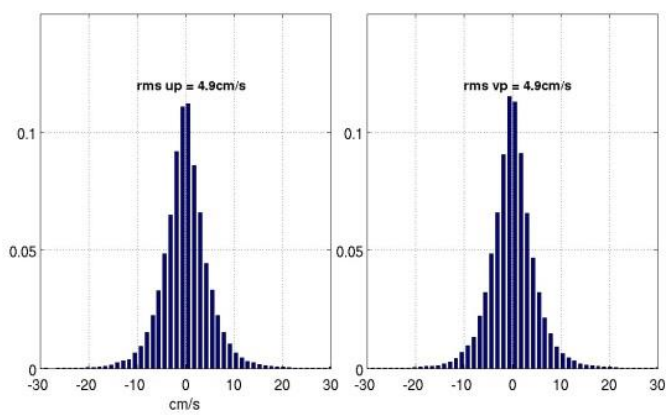
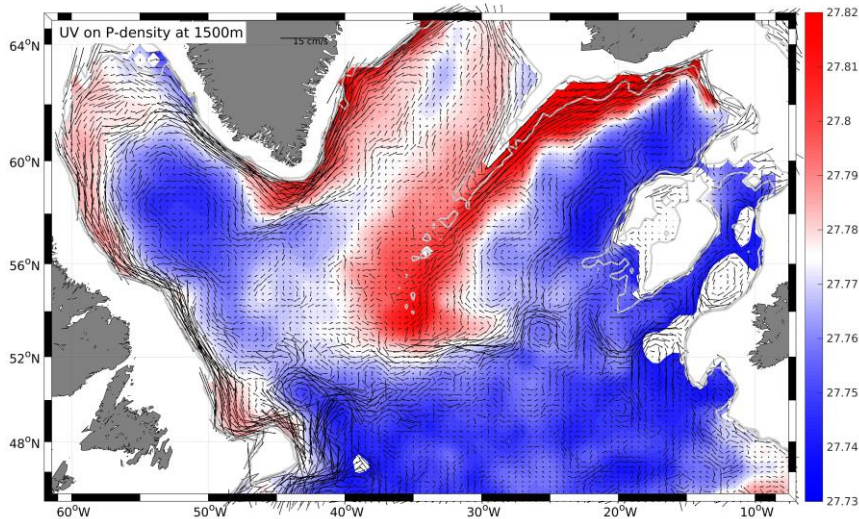


Figure 4: Normalized distribution of the Mid-depth eddy velocity components; left is u' (east-west component) and right is v' (north-south component) – Gaussian distribution with equal rms of 4.9 cm s^{-1}

795

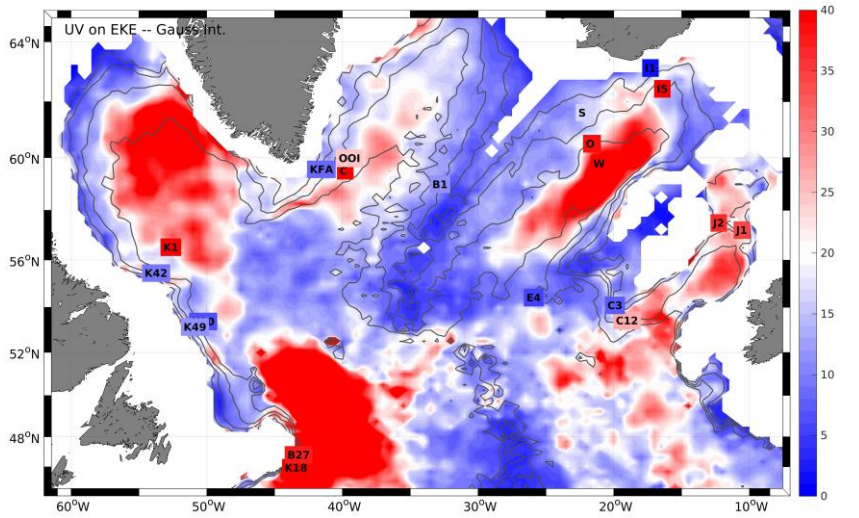
800

805



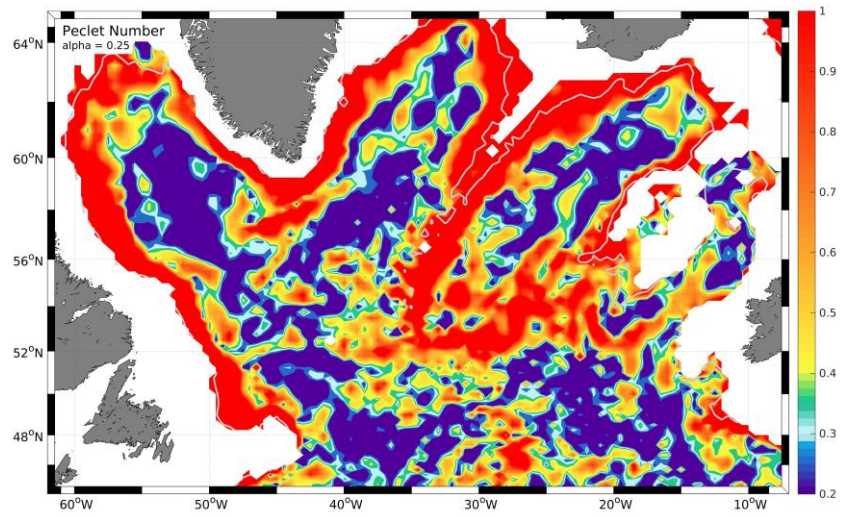
810

815



820

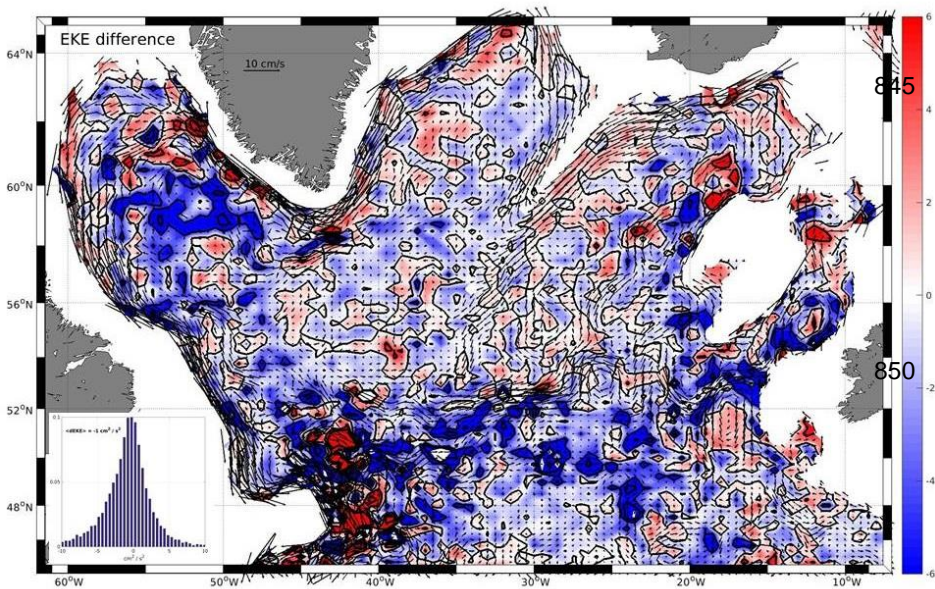
825



830

835 Figure 5 a) Gridded velocity field from the GI method overlaid on potential density distribution from 1500 m depth. b) Gridded EKE (in $\text{cm}^2 \text{s}^{-2}$) map from the GI method with selected EKE values from moored observations (numbers in boxes). Mooring fluctuations are lowpass filtered at 10d cut-off for better comparability of mooring time series with 10 day displacement velocity from Argo data. Mooring location markers are colored with respect to the EKE from the moored record; colormap is identical to that of the background field. c) The ratio of mean speed to the square root of the EKE scaled by a factor $\alpha=0.25$, i.e. a measure of the Peclet number Pe .

840



855 Figure 6: EKE-Map Difference between Optimum Interpolation and Gaussian Interpolation method. Inlet at lower left: Histogram of Difference reveals Gaussian shape and a weak bias of $\langle dEKE \rangle = -1 \text{ cm}^2 \text{ s}^{-2}$

860

865

870

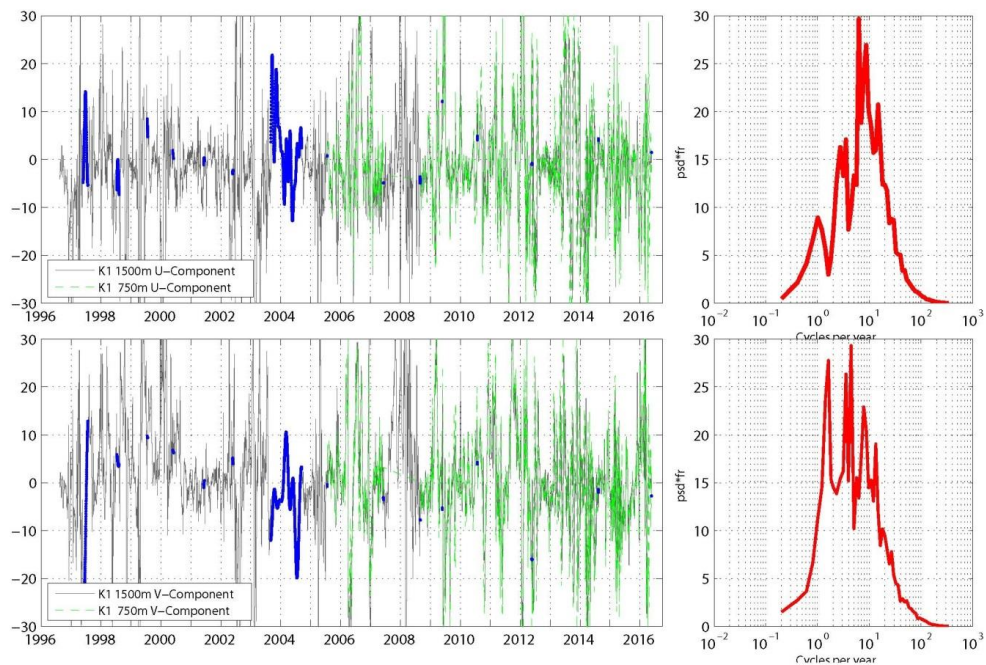
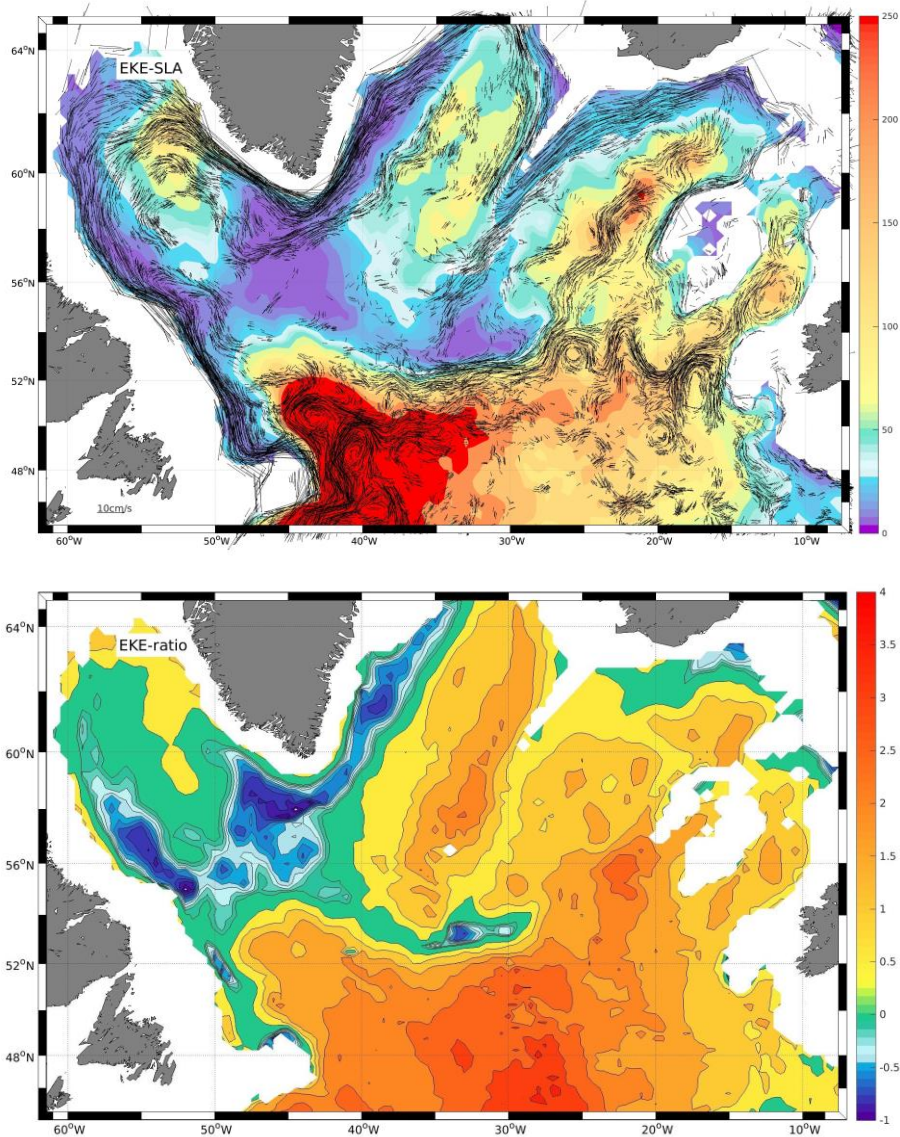


Figure 7: Example of a current time series from the central Labrador Sea at mooring K1. Two depth levels were occupied regularly (750m since 2006 (green curve); 1500 m since 1996). Gaps (blue lines) are filled by EOF based interpolation (Zantopp et al., 2017). High frequency spectra from 1500 m records (right).

875



900

Figure 8: a) Surface EKE derived from the AVISO geostrophic surface flow which is high pass filtered at 180d cut-off (in $\text{cm}^2 \text{s}^{-2}$) as an estimate of the geostrophic turbulence. Overlaid is the Argo derived mean (PV-related) flow at 1000-1500m depth, with flow speeds below 1.5 cm s^{-1} omitted; this better reveals the major advective pathways. b) The logarithmic ratio of surface EKE to deep EKE; green and blue colors show areas in which the deep EKE dominates.

905 **Tables**

Table 1: Eulerian EKE - statistics in the Subpolar North Atlantic. BODC: British Oceanographic Data Centre (www.bodc.ac.uk)

Mooring Nominal instrument depth	latitude	longitude	<Spd> cm s ⁻¹	EKE _{Full} cm ² s ⁻²	EKE _{10dip} cm ² s ⁻²	EKE _{GI} cm ² s ⁻²	Pe	Comment
Moorings in the North West Atlantic								
K42 ₁₅₀₀	55° 27.5'N	53° 43.8'W	16.1	29	6	18	6.6	AR7W mooring
K49 ₁₅₀₀	53° 08.5'N	50° 52.1'W	12.5	39	12	20	3.6	Records from the 53°N observatory
K10 ₁₅₀₀	53° 22.8'N	50° 15.6'W	0.2	13	7	13	0.1	
K1 ₁₅₀₀	56° 31.5'N	52° 39.0'W	1.6	165	72	34	0.2	Mid Basin moorings
CIS ₁₀₀₀	59° 42.7'N	39° 36.2'W	1.6	37	21	20	0.3	
OOI	59° 58.5'N	39° 28.9'W	1.9	63	25	20	0.4	OOI Irminger Sea (access
K18 ₁₅₀₀	46° 27.1'N	43° 25.1'W	4.3	78	50	52	0.6	Flemish Cap Moorings
B227 ₁₁₀₀	47° 06.2'N	43° 13.6'W	27.3	60	38	50	4.3	
B1 ₁₅₃₄	59° 48.5'N	32° 48.5'W	2.1	18	12	13	0.6	Reykjanes Ridge (access via BODC)
KFA	59° 35.0'N	41° 33.0'W		18	9	12		Cape Farewell, NOCS (access via BODC)
Moorings in the North East Atlantic								
I3 ₁₁₃₅	62° 43.1'N	16° 49.2'W	6.1	110	26	16	1.2	Iceland Array (access via BODC)
I5 ₁₄₀₃	62° 26.4'N	16° 28.3'W	3.1	90	54	21	0.4	
S ₁₂₄₅	61° 04.1'N	22° 11.5'W	4.5	47	17	16	1.1	ISOW transport Array
O ₁₄₈₀	60° 30.5'N	21° 36.1'W	4.0	68	39	24	0.6	
W ₁₅₂₀	59° 46.8'N	20° 56.6'W	1.0	133	90	48	0.1	
J1	57° 12.9'N	10° 34.0'W	3.2	41	35	23	0.5	Jasin moorings (access via BODC)
J2	57° 30.1'N	12° 16.0'W	3.3	44	37	22	0.5	
C3 ₁₂₉₀	54° 05.2'N	19° 55.0'W	5.6	15	8	17	2.0	Conslex moorings (access via BODC)
C12 ₁₂₆₀	53° 25.2'N	19° 18.0'W	2.8	35	27	23	0.5	
E4	54° 24.8'N	25° 54.1'W	3.1	7	6	8	1.3	WOCE mooring (access via BODC)